Sensors and Actuators A 223 (2015) 49–60

Contents lists available at ScienceDirect

Sensors and Actuators A: Physical

journal homepage: www.elsevier.com/locate/sna

Dynamic modeling of a bidirectional magnetoelastic rotary micro-motor

Jinhong Qu [a,*], Jun Tang [b], Yogesh B. Gianchandani [a,b], Kenn R. Oldham [a], Scott R. Green [b]

[a] Department of Mechanical Engineering, University of Michigan, Ann Arbor, MI 48109, USA
[b] Department of Electrical Engineering and Computer Science, University of Michigan, Ann Arbor, MI 48109, USA

ARTICLE INFO

Article history:
Received 30 September 2014
Received in revised form 1 December 2014
Accepted 26 December 2014
Available online 4 January 2015

Keywords:
Magnetostrictive
Wireless actuation
Resonant actuation
Modal analysis
Collision model
Transient model

ABSTRACT

A dynamic model is presented for a novel magnetoelastic rotary micro-motor. Magnetoelastic excitation results in a rotary motor with comparatively large payload even under direct wireless actuation, but the resulting stator behavior is significantly different from that of prior micro-scale rotary motors. A parametric modal model is developed from conservation of momentum, a second order linear distributed stator and ballistic rotor motion. The modes and a pre-stressed finite element model are also described to support the parametric modal model. The typical simulated model output and parametric analyses are presented with important trends and behaviors of the micro-motor motion, including stochastic features of rotary and vertical motion, and experimental validation. The dynamics of the micro-motor under certain inputs and design parameters are also estimated by the model.

1. Introduction

Chip-scale rotary micro-motors based on magnetoelastic transduction have recently been demonstrated [1]. These motors join other transduction mechanisms for realizing chip-scale rotary motion, including electrostatic, piezoelectric and others [2,3]. In general, micro-motors based on smart materials and fabricated by MEMS technology have demonstrated better efficiency than chip-scale versions of traditional electromagnetic motors [3].

Chip-scale rotary micro-motors are useful in a broad range of applications [4–8]. One emerging opportunity is to integrate rotary motion with a MEMS gyroscope and control electronics to realize on-chip calibration of long-term gyroscope gain and bias drift [9,10]. However, such an application requires exceptionally high motion accuracies; a representative gyroscope calibration requirement is rotation at up to 1000 degree/s over arbitrary angles with a resolution better than ±10 milli-degrees. To reach such accuracy, the dynamic behavior of a micro-motor must be well understood and distilled into an analytical or numerical model. A model that captures essential behaviors, including transient and steady-state stator motions, stator-to-rotor momentum transfer mechanics, and energy loss mechanisms, is important for predictive design. Such a model is also needed for improving motion estimation accuracy using Kalman filters or other estimation and control schemes. This paper describes the first detailed dynamic modeling of a rotary micro-motor based specifically on magnetoelastic excitation.

Magnetoelastic rotary micro-motors [1] can be driven with a larger payload than other motors at the same scale; this feature is helpful for carrying on-chip gyroscopes for calibration. Magnetoelastic motors can also be remotely, wirelessly actuated without coupling circuitry. The direction of rotation is selected by changing the electromagnetic field input frequency between well-defined resonant modes. The model presented in this paper focuses on a micro-motor designed for the in situ gyroscope calibration task described above. Fig. 1(a) shows a scanning electron microscopy (SEM) image of a magnetoelastic micro-motor stator and Fig. 1(b) shows the schematic of the device.

Many studies have been completed on rotary micro-motor dynamics based on other transduction mechanisms. Electrostatic micro-motors [2,11], for example, have been extensively studied [12–14]. These motors are actuated through non-contact interactions that are significantly different from the stator–rotor interaction in a magnetoelastic micro-motor. Piezoelectric micro-motors are more closely related, being based on contact between stator and rotor, as in the magnetoelastic motor. Many piezoelectric motor models have been proposed; types of these models include: (1) dynamic models based on nonlinear stator–rotor contact, without considering the reaction of the stator to contact with the rotor [15]; (2) models based on the Rayleigh–Ritz assumed

* Corresponding author at: 3632 GGB (George G. Brown Laboratory), 2350 Hayward, Ann Arbor, MI 48109, USA. Tel.: +1 734 353 2760.
E-mail address: jinhongq@umich.edu (J. Qu).

http://dx.doi.org/10.1016/j.sna.2014.12.029
0924-4247/

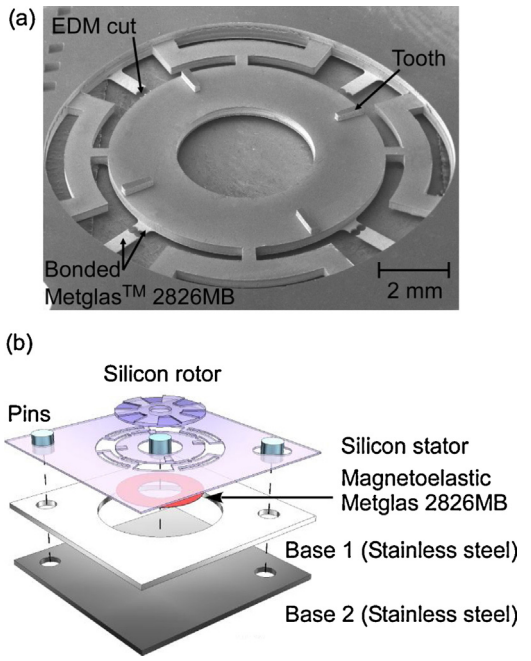

Fig. 1. Prototypes of the magnetoelastic micro-motor (a) SEM of the stator layer; (b) schematic of the magnetoelastic micro-motor.

mode energy method, without considering shear and rotary inertia effects [16]; (3) models applying a linearized impact force as a change in the stator's vibration frequency [17] and (4) finite element methods applied by assuming the stator and rotor are in constant contact [18,19]. The piezoelectric micro-motors described were all designed for traveling wave actuation, which eases control. More recently, nonlinear dynamics of rub-impact-actuated micro-motors have been studied via classical impact theory and dry friction models; however, to date these studies are without experimental validation [20,21].

While both piezoelectric ultrasonic and magnetoelastic motors are actuated by high frequency stator vibration, which makes contact with a rotor, the two most prominent differences are: (1) the forcing mechanism is magnetoelastic rather than piezoelectric, thus relying on in-plane magnetic fields rather than through-the-thickness electric fields, and (2) the suspended nature of the magnetoelastic stator along with the high intended payloads means that the stator motion – not just the rotor motion – is substantially affected by contact interactions. As a result, considering both the driving magnetostrictive force and the stator-to-rotor impacts from the stator perspective can give a better prediction of motor motion than existing micro-motor models. Thus, a model accounting for linear and angular momentum transfer during the contact process has been developed. This is coupled with the rigid body dynamic response of a rotor to model the complete magnetoelastic motor behavior. In the present work, this coupling is analyzed for a standing wave in the stator, which also varies from most prior rotary motor models. Modeling results are presented under various design and operating parameters, and compared to experimental results for a prototype motor.

2. System description

2.1. Device architecture and actuation concept

The micro-motor consists of the following key components (Fig. 1): a stator (with four teeth located on the top surface), a rotor, and a hub. The stator is suspended in a recessed base that allows stator vibration and provides locations for alignment pins and the hub. The stator is a flexible structure that includes a layer of magnetoelastic material, the component driven by the magnetic field directly. For best response, the driving magnetic field should be oriented in the same plane as the magnetoelastic layer. The teeth on the stator transfer energy from stator vibration into the rotation of the rotor. The ring-shaped stator is suspended by four crab-leg springs, which are stiff in the rotational direction but flexible in the out-of-plane direction; these prevent stator rotation during rotor actuation while allowing large vertical deformation required for actuation. The rotor may rotate arbitrarily large angles about the hub, while the hub limits the lateral and/or vertical motion of the rotor.

The generation of rotary motion is similar to that for piezoelectric ultrasonic rotary motors [22]. A vibratory wave, either a standing wave (as in this work) or a traveling wave, is generated in the stator. The resulting vibratory mode shape of the stator has antinodes at which maximal out-of-plane deflection occurs. For the standing wave motor, the teeth are located on the stator such that they are offset from the antinodes, resulting in tangential and vertical motion of the teeth tips. In the design presented, the suspension has two useful modes with different resonant frequencies and antinodes separated by 45°. By selecting either resonant frequency when driving the stator, the tangential direction of the teeth oscillations may be switched, thereby reversing the rotation. When the stator is driven magnetoelastically, a series of collisions between the teeth and the rotor occurs. Because the teeth are moving both vertically and tangentially, each collision will, in general, impart both a vertically oriented and a tangentially oriented impulse force between the contacting teeth and the rotor. Tangential motion from a pair of opposing teeth results in rotation about a central hub, while the vertical motion of the rotor resembles rigid body ballistic motion between collisions. Meanwhile, the impulse force delivered to the stator by the collisions results in a transient dynamic response superposed with the steady-state resonant response.

2.2. Device fabrication

The stator and rotor are fabricated side-by-side from a 350 μm thick silicon wafer using a two-mask deep reactive-ion etching (DRIE) process. At the end of this process, the ring-shaped stator is fully etched out, and the teeth are defined on the top surface of the stator. The silicon rotor has a through hole at the center for placement on the hub.

The magnetoelastic layer is batch-patterned using photochemical machining (PCM) [23] from Metglas™ 2826MB foil, a nickel–iron–molybdenum–boron alloy with desirable magnetostrictive properties [24]. The ring-shaped stator is patterned with an inner diameter of 4 mm and an outer diameter of 8 mm, and with a thickness of 25 μm. The ring is held in a frame by simple connecting tethers. The recessed base is formed using two layers that are also fabricated using PCM from 0.5 mm thick stainless steel foils.

The patterned Metglas™ 2826MB foil is bonded to the silicon stator using Au–In transient liquid phase bonding (TLP) [25,26]. After bonding, the connections between the ring and frame in the Metglas™ 2826MB layer are cut using micro-electro-discharge machining [27]. An SEM image of the silicon stator with bonded ring-shaped Metglas™ 2826MB is shown in Fig. 1(a). As the final step before testing, the silicon stator, stainless steel bases, and a hub (ø2 mm stainless steel pin) are aligned, stacked and fixed to each other with epoxy. The silicon rotor is placed directly above the stator and is constrained by the hub while touching the stator only at the teeth.

3. Dynamic rotary motor model

3.1. Modeling approach and setup

3.1.1. Modeling method

To understand and predict the dynamic motion of the motor, both a parametric modal model (PMM) and a finite element model (FEM) are used. The PMM is based on geometric parameters and physical properties of the stator and rotor (certain of which must be measured experimentally), which can be used to predict the dynamic motion of the motor. The PMM captures the major features of the motor motion, and is especially useful in simulating long durations of operation with many stator-to-rotor collisions. The FEM is based on a COMSOL Multiphysics model and is used to predict additional behavior of the stator, including mode shapes, driven stator amplitude, and residual deformation from fabrication processes. It is helpful to predict stator motion before fabrication and serves to validate some assumptions used in the PMM.

3.1.2. Finite element model

A custom magneto-mechanical finite element technique is used to estimate modal displacements, shapes, and frequencies for the stator when driven with a magnetic field. Although magnetoelastic materials are generally non-linear, it is appropriate in this application to use linearized constitutive equations describing the coupling between flux, field strength, stress, and strain in a magnetostrictive material,

$$\vec{\sigma} = [C]\vec{\varepsilon} - \frac{[C][d]^T}{\mu_0\mu_r}\vec{B} \quad (1)$$

$$\vec{H} = -\frac{[d][C]}{\mu_0\mu_r}\vec{\varepsilon} + \frac{1}{\mu_0\mu_r}\vec{B} \quad (2)$$

where σ is the stress vector, C is the stiffness matrix, ε is the strain, d is the magnetostrictivity matrix, B is the magnetic flux density vector, H is the field strength vector, μ_0 is the permeability of free space, and μ_r is the relative permeability. Eqs. (1) and (2) are implemented in this work utilizing COMSOL Multiphysics 4.3 with solid mechanics and magnetic field physics domains. A detailed look at a FEM implementation for magnetostrictive materials is presented in [28]; the approach used in this work is modified for application to resonant actuators. This coupled FEM is used to evaluate a number of stator behaviors used in the dynamic PMM, including:

1. Deformation due to thermal expansion mismatch between the silicon and Metglas™ layers.
2. Eigenfrequencies and mode shapes of the stator (both with and without thermal expansion deformation).
3. Magnetomechanical response of the stator (again, with and without thermal expansion deformation).
4. Impulse response of the stator.

In contrast, sustained motion over many impacts is better described by the PMM, using the above information from the FEM or from experimental measurements. For predictive design, the target stator geometry can be implemented in the FEM model and analyzed. For model verification, the measured stator geometry is implemented and analyzed.

3.1.3. PMM assumptions

In addition to information from the FEM, the following assumptions are made in deriving the dynamic PMM:

1. Teeth are treated as rectangular bodies with a negligible moment of inertia.
2. Collisions occur at the inner edges of the teeth.

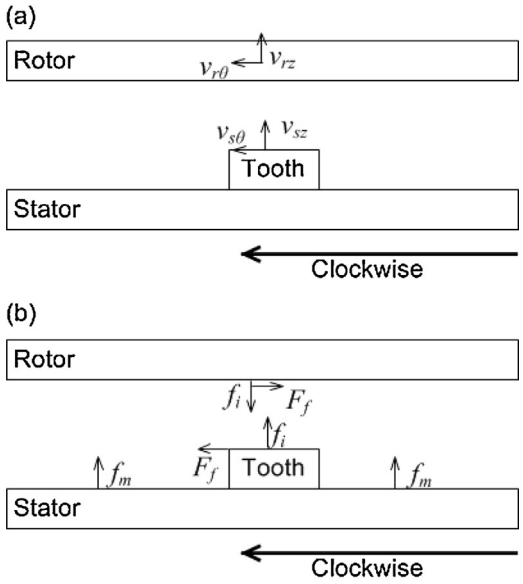

Fig. 2. (a) Velocity definitions and (b) forces acting on the micro-motor.

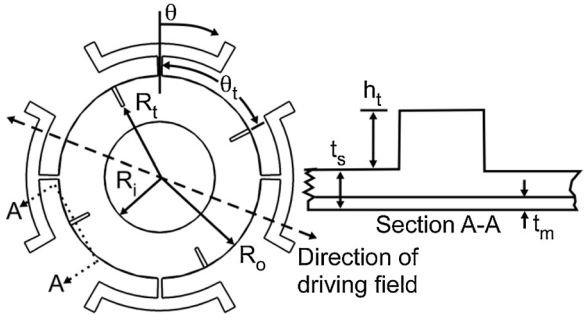

Fig. 3. Stator geometry and key dimensional parameters.

3. During contact, slippage could occur between the teeth and the rotor. If slippage is calculated to occur (based on the contact angle), the tangential force is proportional to the normal force (i.e. a dry Coulomb friction model).
4. A pair of teeth, each tooth located on opposite sides of the stator, collides with the rotor at the same time with identical velocities. (Some randomness in the vibration amplitude of each pair of teeth will later be introduced to account for non-uniformity of the fabricated system.)
5. The mass distribution of the stator is uniform.
6. The damping coefficients and spring rates of the stator are mode-dependent constants.

3.1.4. Variable definitions

Variables used in the dynamic PMM are introduced here (Fig. 2). First, the velocities of the stator teeth, denoted by subscript s, and rotor, denoted by subscript r, are defined as shown in Fig. 3, in tangential (θ) and vertical (z) directions. Velocities before collisions are further denoted by subscript o, after collision by subscript f, and in steady-state (no rotor or collisions) by subscript ss. Four different forces are defined. F_f is the friction between the stator and rotor in the tangential direction and F_n is the normal force between the stator and rotor in the vertical direction. f_m is the magnetic force acting on the stator, generated by the coils, resulting in the out-of-plane driven stator motion. f_i is the impulse force, and appears only when a vertical collision occurs between the stator and rotor. In this case, $F_n = f_i$. Finally, $u(\theta,t)$ is defined as the distributed vertical

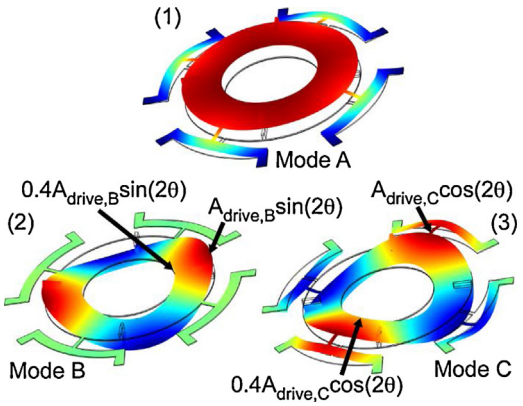

Fig. 4. The modes of the motor: (1) pseudo-rigid-body mode (first mode, mode A); (2) first actuation mode (fourth mode, mode B) and (3) second actuation mode (fifth mode, mode C).

displacement of the stator as a function of time (t) at the angular position on the stator (θ).

3.1.5. Stator geometry and dynamics

Geometric parameters describing the stator are illustrated in Fig. 3. These include stator radii (inner, R_i, outer, R_o, and inside of teeth, R_t), and tooth angular locations, θ_t. The teeth are offset from the locations of maximum motion for both actuation modes, so that the teeth will move in opposite directions in the two actuation modes.

3.2. Dynamic model derivation

3.2.1. FEM results: resonant mode shapes, static deformation and mode misalignment

The dynamic PMM is based on a stator undergoing a magnetoelastically driven standing wave, with transient effects introduced by impact events with the rotor. Via the applied magnetic field or as a result of collisions between the teeth and the rotor, different vibration modes can be excited (Fig. 4). The excited mode with the lowest frequency, referred to as mode A in this paper, is a pseudo-rigid-body motion of the entire stator ring. The magnetoelastically driven modes are those used to generate the rotary motion and are referred to as modes B and C in this paper. Two other tilting modes exist between mode A and modes B and C; however, these are not strongly excited by the symmetric collisions and driving magnetic field. In the prototype micro-motor studied, mode B occurs at about 6.3 kHz and has its maximum vibration position located between the suspension connections; this mode shape causes the rotor to rotate clockwise. Mode C occurs at about 7.4 kHz and has its maximum vibration position at the connections of the stator to the suspension; mode C causes the rotor to rotate counter-clockwise.

Eigenfrequencies, mode shapes, and damping ratios for the stator can also be calculated using the FEM. Modes B and C are excited by a driving magnetic field, which is implemented by assigning a surface current to the curved surface of a cylindrical domain positioned around the stator, with the long axis of the cylinder in the direction of the driving field. The surface current density amplitude is specified such that the resulting magnetic field amplitude is the same as that generated by the Helmholtz coils at the position of the motor. Mode A is excited via a periodic force applied to the top surfaces of the teeth. A frequency sweep analysis is performed near the eigenfrequencies of interest to estimate the steady-state amplitude of the driven mode shapes, and to estimate the quality factor (and associated damping ratio) of the resonant peaks.

The Au–In eutectic formed during the bonding process described in Section 2.2 solidifies at approximately 157 °C [25,26]. The thermal expansion mismatch of the bonded silicon (2.6 ppm/°C) and Metglas™ (11.7 ppm/°C) layers results in tensile stress in the Metglas™ layer once the laminate is at room temperature. This stress is partially relieved through out-of-plane bending of the stator. The deformation resulting from this thermal expansion mismatch can also be predicted using the FEM. The expected out-of-plane displacements due to thermal expansion mismatch are comparable to the thickness of the stator. The calculated deformation for the geometry investigated in this work shows a 77 μm difference in out-of-plane deflection from the inner radius to the outer radius of the stator, with the maximum deflection occurring at the inner radius of the stator. This compares well with the interferometer-measured (Olympus LEXT) deformation of the as-fabricated device, which showed a 70 μm difference at comparable positions. The residual deformation leads to the assumption that the collision between stator and rotor happens at the inner edge of the teeth.

An analysis of the unstressed stator (neglecting thermal expansion mismatch) and an analysis of the pre-stressed stator were performed. Calculated mode shapes, evaluated as displacements from the unstressed or pre-stressed state, were identical for both analyses; however, the pre-stressed eigenfrequency analysis exhibited higher modal frequencies for each shape. Therefore, the eigenfrequencies of the stator used in this paper are measured experimentally. It was also found that the driven amplitudes, mode shapes, and quality factors were not significantly different between unstressed and pre-stressed analyses.

The FEM also illustrates the effect of small geometrical and material asymmetries on the exact mode shape. For instance, even with a symmetric geometry that is meshed slightly asymmetrically, it was found that the mode shapes of mode B and mode C shifted by ≈2° in the same direction. Small geometrical asymmetries are expected in the fabricated devices as well; thus, the angle by which the mode shapes have shifted is later used as a tuning parameter in the model to match the experimental results. The expected possible range of shift angle is ±3°.

3.2.2. Stator model

The stator is treated as a ring with uniform mass distribution. Once the inertia of the teeth is assumed to be negligible, it is reasonable to model the stator as a linear mass–spring–damper system with respect to angle (θ) and time (t):

$$m\ddot{u}(\theta, t) + b(\theta)\dot{u}(\theta, t) + k(\theta)u(\theta, t) = f_m + f_i \tag{3}$$

in which mass (m), damping coefficient (b), the spring constant (k), and both forces f_m (magnetic force from the coil) and f_i (impulse force from rotor) are given in units per angle. For example, m is defined as $m_s/2\pi$, in which m_s is the mass of the stator.

The stator displacement at the inner tooth radius (R_t) as a function of time and angle ($u(\theta,t)$) can be decoupled into a combination of the three previously described modes,

$$u(\theta, t) = g_A(t) + g_B(t)\sin(2\theta) + g_C(t)\cos(2\theta). \tag{4}$$

The actuation (magnetic) force can also be modeled over the two excitation modes as,

$$f_m(\theta, t) = f_{mB}\sin(2\theta)\sin(2\pi f_B t) + f_{mC}\cos(2\theta)\sin(2\pi f_C t) \tag{5}$$

in which f_B and f_C are the actuation frequencies and either f_{mB} or f_{mC} (amplitude of the magnetic force) is set to be zero because only a single frequency will be used to actuate the device at any given time.

The interaction force between the stator and the rotor, acting on the stator, can be determined by linear momentum conservation at the rotor. Describing the impulse force f_i as force per angle, the

expression for momentum transfer in the vertical direction from a collision between the rotor and stator is as follows:

$$f_i = -\frac{m_r(v_{rf} - v_{ro})\delta(t - t_c)}{2\Delta\theta} \tag{6a}$$

Here, the interaction force is placed at tooth position θ_t and determined by the rotor velocity before (v_{ro}) and after (v_{rf}) collision. $\delta(t-t_c)$ is the Dirac delta function defined to occur at the collision time (t_c). When wobble and tilting of the rotor are insignificant, the two teeth in each set are assumed to collide identically with the rotor. The interaction force is assumed to act on the entire arc length of the tooth in the angular direction at its lateral surface, occupying angle $\Delta\theta$. Therefore the force can be expressed as a function of a pulse train having amplitude $-1/2[m_r(v_{rf}-v_{ro})]$ and spatial duty cycle θ and period π.

Expanding that spatial distribution of the interaction force in a Fourier series, the spatial distribution of the impulse force is a summation of a spatially independent term and an infinite number of terms that are circumferentially periodic. Thus, the only mode shapes that are excited by such a force are modes A, B and C as described previously, as well as higher order modes with an even number of antinodes. The terms relating to these higher order modes are neglected, as their high resonant frequencies result in negligible displacement amplitudes relative to modes A–C. The interaction force is thus reduced from (6a), for $\Delta\theta \ll \pi$, to:

$$f_i \approx -\frac{1}{2}m_r(v_{rf} - v_{ro})\delta(t - t_c) \times \left[\frac{1}{\pi} + \frac{2}{\pi}\cos(2\theta)\cos(2\theta_t) + \sin(2\theta)\sin(2\theta_t)\right] \tag{6b}$$

From the assumption that the damping coefficient (b) and the spring constant (k) are mode dependent constants, the second order linear equation of the stator can be decoupled into three second order linear differential equations in time, one per mode shape, with different damping coefficients and spring constants. Substituting (4), (5) and (6b) into (3) and decoupling:

$$m\ddot{g}_A(t) + b_A\dot{g}_A(t) + k_A g_A(t) = -\frac{1}{2\pi}m_r(v_{rzf} - v_{rzo})\delta(t - t_c) \tag{7a}$$

$$m\ddot{g}_B(t) + b_B\dot{g}_B(t) + k_B g_B(t) = -\frac{1}{\pi}m_r(v_{rzf} - v_{rzo})\delta(t - t_c)\sin(2\theta_t) + f_{mB}\sin(2\pi f_B t) \tag{7b}$$

$$m\ddot{g}_C(t) + b_C\dot{g}_C(t) + k_C g_C(t) = -\frac{1}{\pi}m_r(v_{rzf} - v_{rzo})\delta(t - t_c)\cos(2\theta_t) + f_{mC}\sin(2\pi f_C t) \tag{7c}$$

The response of each equation can be superposed as the sum of responses under the magnetic force and interaction forces. The magnetic force produces the steady-state stator response to a second order linear equation and the interaction force response is the impulse response.

Solving (7a)–(7c), the steady-state motion in the vertical direction is:

$$u_{ss}(\theta, t) = \begin{cases} A_B\sin(2\theta)\sin(2\pi f t) & \text{mode B} \\ A_C\cos(2\theta)\sin(2\pi f t) & \text{mode C} \end{cases} \tag{8a}$$

in which A_B and A_C are the vertical steady state motion amplitudes.

Meanwhile, the vertical displacement response when collisions occur is modeled as the sum of the impulse responses of each mode shape (7a)–(7c):

$$u_i(\theta, t) = \frac{2\pi F_n}{m_s\omega_{d,A}}e^{-\xi_A\omega_A t}\sin(\omega_{d,A}t) + \frac{4\pi F_n}{m_s\omega_{d,B}}e^{-\xi_B\omega_B t}\sin(\omega_{d,B}t)\sin(2\theta_t)\sin(2\theta) + \frac{4\pi F_n}{m_s\omega_{d,C}}e^{-\xi_C\omega_C t}\sin(\omega_{d,C}t)\cos(2\theta_t)\cos(2\theta) \tag{8b}$$

in which, from integrating (6b) over time at $\theta = \theta_t$,

$$F_n = -\frac{1}{2}m_r(v_{rf} - v_{ro})\frac{1}{\pi} \tag{8c}$$

and $\omega_n = 2\pi f_n = \sqrt{\frac{k_n}{m}}$, $\omega_{d,n} = \omega_n\sqrt{1-\xi_n}$, $\xi_n = \frac{b_n}{2m\omega_n}$, and $n = A$, B or C.

Likewise, the tangential response can be found as a combination of three responses. During vibration, the tooth tilts through an angle of amplitude θ_{tilt}. Because the vertical and the tangential motion of the tooth are related through the rigid geometry of the tooth, the tangential motions in the clockwise direction of the stator at the tooth position can be obtained from the derivative of vertical motion with respect to rotor angle ($\partial u/\partial\theta$), giving:

$$u_{ss,tangential}(\theta, t) = \left(\frac{t_s}{2} + h_t\right)\sin(\theta_{tilt}) \approx \left(\frac{t_s}{2} + h_t\right)\frac{\partial u_s(\theta, t)}{\partial r\theta} = \begin{cases} A_B\dfrac{(t_s + 2h_t)}{r}\cos(2\theta)\sin(2\pi f t) & \text{mode B} \\ -A_C\dfrac{(t_s + 2h_t)}{r}\sin(2\theta)\sin(2\pi f t) & \text{mode C} \end{cases} \tag{9a}$$

(9b) $u_{i,tangential}(t)\left(\frac{t_s}{2} + h_t\right)\sin(\theta_{tilt}) \approx \left(\frac{t_s}{2} + h_t\right)\frac{\partial u_i(\theta,t)}{\partial r\theta} = \frac{4\pi F_n}{m_s\omega_{d,B}}\frac{(t_s+2h_t)}{r}e^{-\xi_B\omega_B t}\sin(\omega_{d,B}t)\cos(2\theta_t) - \frac{4\pi F_n}{m_s\omega_{d,C}}\frac{(t_s+2h_t)}{r}e^{-\xi_C\omega_C t}\sin(\omega_{d,C}t)\cos(2\theta_t)\sin(2\theta)$

3.3. Collision model

To complete the collision model, the coefficients of restitution and friction are defined.

Coefficient of restitution: the coefficient of restitution is defined as the ratio of the relative velocity in the normal direction after collision to the relative velocity in the vertical direction after collision.

$$e = \frac{v_{rzf} - v_{szf}}{v_{szo} - v_{rzo}}. \tag{10}$$

Coefficient of friction: a dry (Coulomb) friction model is assumed making the relationship between the (vertical) normal force (F_n) and the (tangential) friction force (F_f),

$$F_f = \begin{cases} \mu F_n & \text{if } \mu < \tan(\alpha) \\ \tan(\alpha) & \text{if } \mu > \tan(\alpha) \end{cases} \tag{11}$$

in which μ is defined as the coefficient of friction, and α is the angle between the vertical direction and the interaction force acting on the rotor. The α at each collision is defined as the ratio of the tangential and vertical displacement of the stator at the tooth position. Alternative friction models were also considered [20,29–31], but it was found that these more complex models did not significantly affect the outcome of the model.

3.4. Rotor dynamics

After determining the analytical solution of the stator motion, the change of velocity at the tooth position (θ_t) from before to after

a collision can be derived from (8b) in analytical form:

$$\delta\dot{u}_i(\theta_t, 0) = \frac{2\pi F_n}{m_s} + \frac{4\pi F_n}{m_s}\sin^2(2\theta_t) + \frac{4\pi F_n}{m_s}\cos^2(2\theta_t) = \frac{2\pi F_n}{m_s} + \frac{4\pi F_n}{m_s} \quad (12a)$$

Substituting (12a) into (8c) and defining a mass ratio, r_m, as $3m_r/m_s$, the relation between the velocities of the stator/rotor before/after collision becomes:

$$(v_{szf} - v_{szo}) = \delta\dot{u}_i(\theta_t, 0) = -r_m(v_{rzf} - v_{rzo}) \quad (12b)$$

Given the definition of the coefficient of restitution from (10) and (12b), the expression for v_{szf} (stator velocity after collision at tooth position) and v_{rf} can be derived:

$$v_{szf} = \frac{v_{szo} - r_m\,(ev_{szo} - (e+1)v_{rzo})}{1 + r_m} \quad (13a)$$

$$v_{rzf} = e(v_{szo} - v_{rzo}) + v_{szf} \quad (13b)$$

Finally, the tangential velocity of the rotor after collision, $v_{r\theta f}$, can also be written as a function of the tangential velocity of the rotor before collision, $v_{r\theta o}$, depending on whether the friction exceeds the maximum allowance:

$$v_{r\theta f} = \begin{cases} v_{r\theta o} + \dfrac{\mu m_r(v_{rzf} - v_{rzo})r}{J} & \text{if } \mu < \tan(\alpha) \\ v_{r\theta o} + \dfrac{\tan(\alpha) m_r(v_{rzf} - v_{rzo})r}{J} & \text{if } \mu > \tan(\alpha) \end{cases} \quad (13c)$$

To verify the appropriateness of the above approach, the FEM model was used. The transient response of the stator to a single collision is simulated by applying identical downward Gaussian impulses to the top surfaces of the two colliding teeth in a time domain analysis. The response of the stator is calculated and compared to the impulse response predicted by the PMM with identical parameters to those of the FEM; this comparison shows excellent agreement. This agreement and the PMM's relative computational efficiency explain the utility of the PMM in simulating large rotor motions where many hundreds of stator–rotor collisions occur.

In the basic actuator, the rotor is just an annulus with some small features on the top surface for optical testing purposes, so only the mass (m_r) and the radius of the collision point (r, the same as the radius of collision position on stator) are considered in the vertical direction model and the moment of inertia (J_r) in the tangential direction.

After a collision, the transient motion of the rotor is a ballistic motion affected by the gravity force, squeeze film damping force and the drag force. The upward and clockwise directions are defined as positive vertical and tangential motion. The vertical velocity (v_{rz}) and tangential velocity ($v_{r\theta}$) can be written as follows:

$$m_r\dot{v}_{rz} = -m_r g - b_z v_{rz} \quad (14a)$$

$$J_r\dot{\omega}_{r\theta} = -b_\theta\omega_{r\theta} \quad \text{with} \quad \alpha_{r\theta} = \dot{\omega}_{r\theta} \quad \omega_{r\theta} = \frac{v_{r\theta}}{r} \quad (14b)$$

in which b_z and b_θ are the damping coefficients in the vertical and tangential directions.

3.5. Parameter identification

Before the PMM can generate numerical results, several system parameters must be defined. Parameters can be determined either from prior literature, such as coefficient of restitution and coefficient of friction, or experimentally, such as rotor mass or stator steady-state vibration amplitude. If the model is to be used predictively, the stator vibration characteristics and associated parameters can be estimated using the FEM.

3.5.1. Coefficient of restitution

In general, coefficients of restitution may range from 0 to 1. These coefficients depend on the speed of collision, the materials, and the geometries of the surfaces involved in the collision. Previous studies have shown the coefficient of restitution of collisions between poly-silicon and silicon micro-geometries to range from 0.57 to 0.642 [32,33]. Within that range, coefficient of restitution can be used as a tuning parameter to better match the measured results.

3.5.2. Coefficient of friction

The coefficient of friction (μ) for silicon-on-silicon interaction has been shown to vary widely depending on the exact conditions of the interaction, from 0.03 to 0.69 [34,35]. This coefficient thus can also be considered as a tuning parameter for this model.

3.5.3. Rotor mass

The mass of the rotor can be measured accurately as a discrete component. It is measured to be 46 ± 0.5 mg. The mass of the stator is estimated from the stator geometry to be 10.7 mg.

3.5.4. Squeeze film damping and drag coefficients

From previous literature, squeeze film damping coefficient (damping coefficient b_z) can be approximated by a few different models [36,37]. First, from [36], b_z is estimated at 0.6 mNs/m. b_z, while from [37], at about 3.6 mNs/m. Due to the wide range of reasonable damping coefficients, this parameter was also treated as a tuning parameter for the model.

The viscous drag coefficient (drag coefficient b_θ) from air acting to oppose tangential motion was estimated to be 43 pNs/m, by integrating drag forces about the circumference of the hub [38].

3.5.5. Mode shift

The modes of the stator can be shifted in orientation by asymmetries in stator fabrication or the materials themselves. Because the exact value of this shift could not be measured accurately; an estimated range of the mode shift angle (θ_m) is given as -3 to $+3^\circ$ based on the FEM results shown in Section 4.2. θ_m is defined to be positive in the counterclockwise direction. The shift would be same for both actuation modes. In simulation, θ_m is picked to be -2.5°.

For the prototype motor, the steady-state motion of the stator in magnetic field can be measured experimentally, rather than estimated from the FEM. The mode frequencies and amplitudes of the stator are measured experimentally by giving a frequency sweep to the sinusoidal voltage input and measuring the motion response of the stator.

The full description of the system parameters obtained is shown in Table 1(a–c). The values of parameters used in nominal simulations are listed as "Nom" and their variation.

3.6. Simulation features

Using the parameters in Table 1(a–c), simulation code was implemented in MATLAB to predict dynamic motor behavior. The simulation includes a 0.5% random variation in stator vibration amplitude, similar to that measured from an unloaded stator using Laser Doppler Vibrometry (LDV). Figs. 5–10 show sample results from the simulated rotor motion. The vertical motion of the rotor can be recognized as a ballistic motion between collisions (Figs. 5 and 6), with the vertical velocity having a sudden change at impacts and otherwise affected only by gravity and squeeze-film damping. The tangential velocity increases from rest at the beginning of the simulation and eventually oscillates around a stable value (Fig. 7).

Table 1

(a) Motor geometric parameters in simulation

Parameter (symbol)	Nom (var)	Method
Stator inner radius (R_i)	2.125 (±0.02) mm	M
Stator outer radius (R_o)	3.89 (±0.02) mm	M
Tooth inner radius (R_t)	3.063 (±0.02) mm	M
Stator thickness (t_s)	70 (±10) μm	M
Tooth height (h_t)	260 (±10) μm	M
Tooth location angle (θ_t)	62.635 (±0.2)°	M
Mode shift angle (θ_m)	−2.5°	E

(b) Motor parameters of frequency response in simulation

Parameter (symbol)	Nom (var)	Method
Mode A frequency (f_A)	2150 (±10) Hz	FEM
Mode A damping ratio (ξ_A)	22.5 (±1.4) mN/m	FEM
Mode B frequency (f_B)	6.30 (±0.01) kHz	M
Mode B tooth amplitude	20.72 (±1.24) μm	M
Mode C frequency (f_C)	7.46 (±0.01) kHz	M
Mode C tooth amplitude	1.81 (±0.11) μm	M
Mode B & C damping ratio (ξ_B, ξ_C)	ξ_B 0.0063 (±0.002) ξ_C 0.0075 (±0.002)	M

(c) Motor properties used in simulation

Parameter (symbol)	Nom (var)	Method
Rotor mass (m_r)	46 (±0.5) mg	M
Stator mass (m_s)	10.7 (±1.0) mg	C
Coefficient of restitution (e)	0.6 (±0.04)	[32,33]
Coefficient of friction (μ)	0.4 (±0.37)	[34,35]
Damping coefficient (b_z)	3.6 mNs/m	C
Drag coefficient (b_θ)	4.3×10^{-11} Ns/m	C

Methods used to determine parameter values are denoted as "M" for measured, "E" for estimated and "C" for calculated.

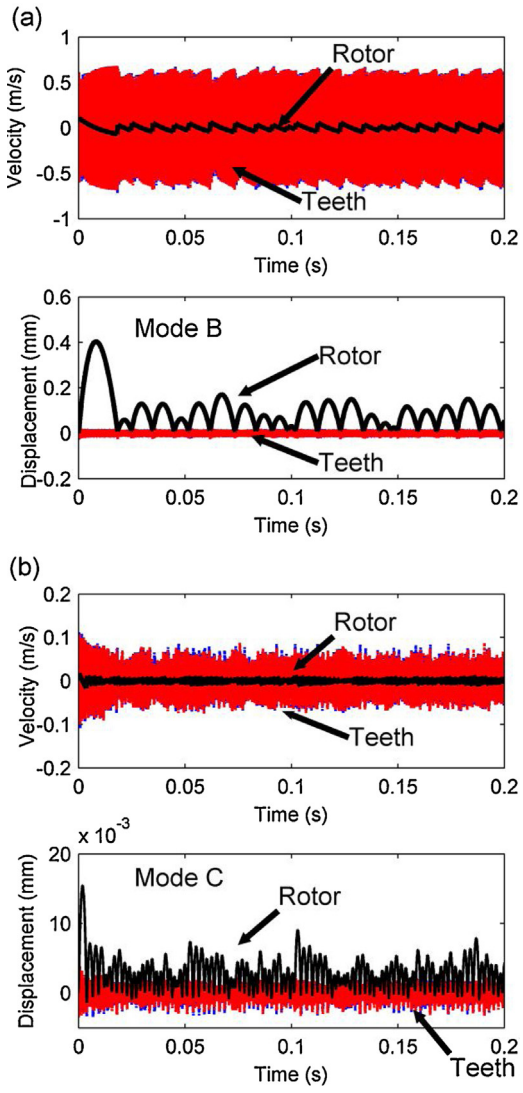

Fig. 5. Sample simulation of vertical velocity and displacement in the time domain: (a) mode B and (b) mode C.

3.7. Parameter sensitivity analysis

As noted above, exact values for some parameters in the model are unknown, such as coefficients of restitution and friction. In addition, it is desirable to understand the effect of parameters over which the motor designer has control. By tuning the parameters over their possible range, it is possible to check which dominates the system performance. When checking the influence of single parameter, all the other parameters are held constant at the nominal value (Table 1). For conciseness, only effects on mode C are presented here. Mode C is selected because this mode has smaller stator vibration amplitude, which in practice reduces the rotor wobble and tilt, the effects of which are not included in the model. The results (Table 2) show the sensitivity of the model output to the parameters of interest. The average and standard deviation of the output reported in Table 2 are calculated from five simulations, each with a random 0.5% variation in stator vibration amplitude. According to the simulations, increasing the stator mass will reduce the

Table 2
Comparison of vibration mode C simulation results under different value of parameters.

Parameter (symbol)	Parameter value	Collision frequency (Hz)	Tangential velocity (rad/s)
Output with nominal parameter values	See Table 1	448 ± 22	1.72 ± 0.09
Stator mass (m_s)	9.7 mg	591 ± 170	1.36 ± 0.17
	11.7 mg	402 ± 36	1.96 ± 0.15
Stator thickness (t_s)	60 μm	434 ± 72	1.67 ± 0.13
	80 μm	440 ± 42	1.72 ± 0.10
Tooth height (h_t)	250 μm	440 ± 32	1.67 ± 0.13
	270 μm	432 ± 52	1.75 ± 0.16
Coefficient of restitution (e)	0.57	450 ± 37	1.73 ± 0.15
	0.642	413 ± 55	1.64 ± 0.07
Coefficient of friction (μ)	0.03	430 ± 49	1.80 ± 0.07
	0.69	430 ± 20	1.68 ± 0.18
Squeeze film damping coefficient (b_z)	0.6 mNs/m	416 ± 59	1.72 ± 0.13
	3.6 mNs/m	448 ± 22	1.72 ± 0.09

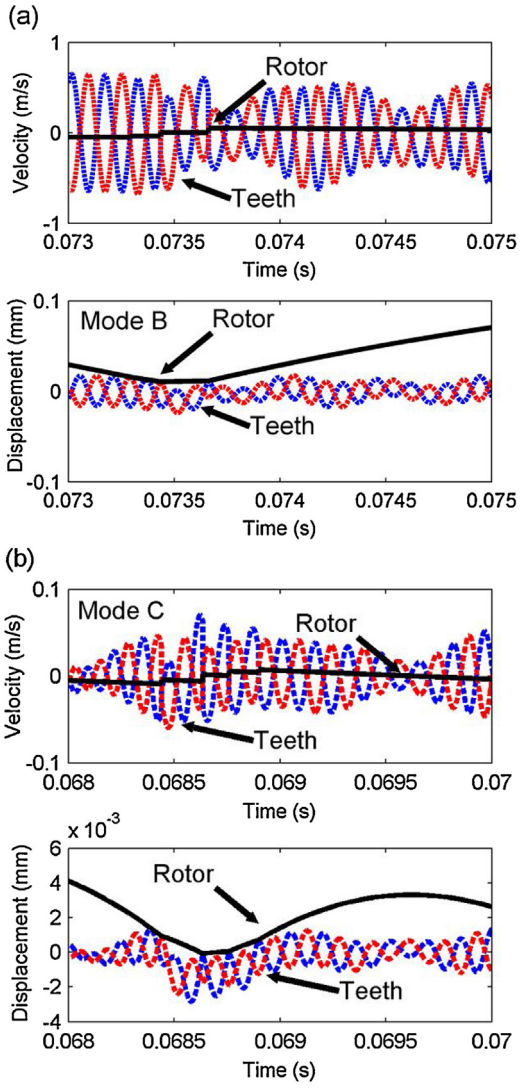

Fig. 6. Detail view of simulation in the time domain: (a) mode B and (b) mode C.

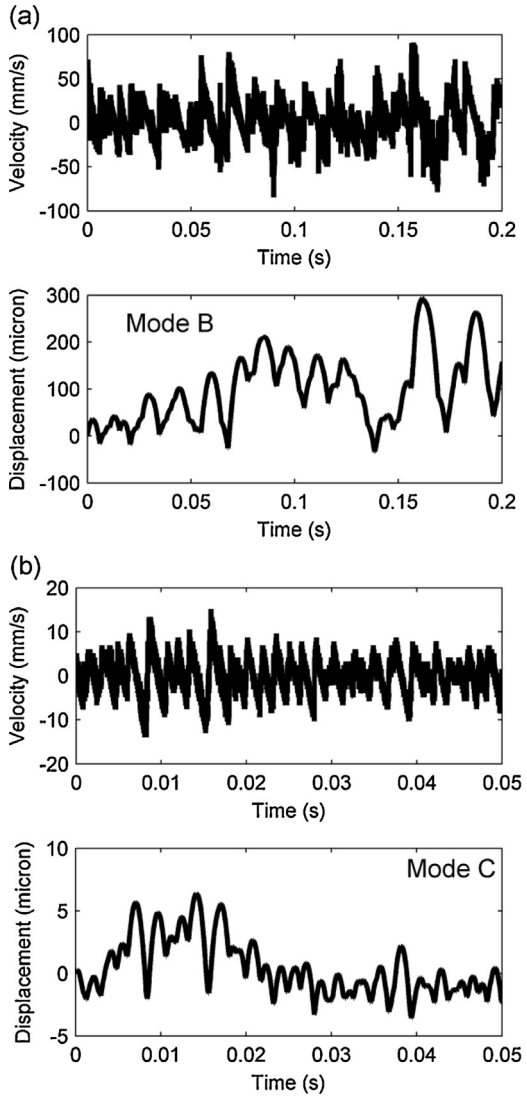

Fig. 8. Typical time domain experimental velocity and displacement under (a) mode B and (b) mode C.

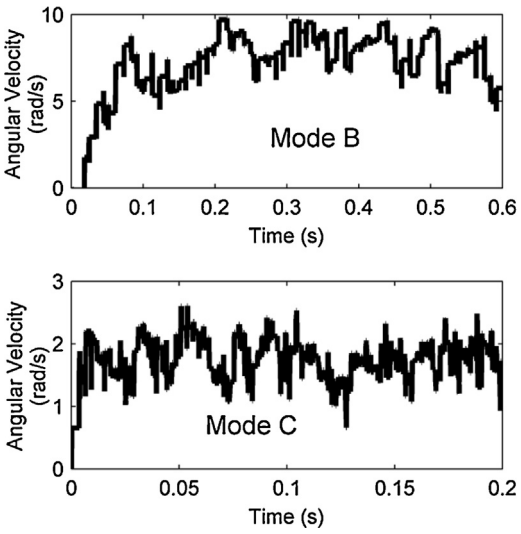

Fig. 7. Sample simulations of angular velocity of the rotor (mode B and mode C).

collision frequency but increase tangential velocity, with greater energy imparted on the rotor at each impact. In reality, the stator thickness and tooth height both affect the stator mass; however, in the trend analysis these parameters are treated as independent and tuned separately to better understand physical behavior. Thus, while increasing stator thickness (and thus stiffness) without increasing stator mass has only a minor effect on performance, in practice increasing stator thickness would also lead to larger stator mass, with the effects noted above. Other parameters in Table 2 show much smaller effects on motor performance.

An additional factor that influences rotor behavior substantially is the position of the rotor teeth with respect to the stator mode shapes of mode B and mode C. If the tooth position is not accurately aligned with respect to its actuation mode, the simulation will give significantly different results. This misalignment can be due to fabrication errors (photolithography mask misalignment, non-uniform etching, over-etching, etc.) and can be represented in the model with either a deviation from the designed tooth angle or with a deviation of the location of the mode shape antinodes from their ideal location. Because both tooth location angle (θ_t) and mode shift angle (θ_m) will affect the model output in the same way, the sum of the angles is considered. For example, in mode B,

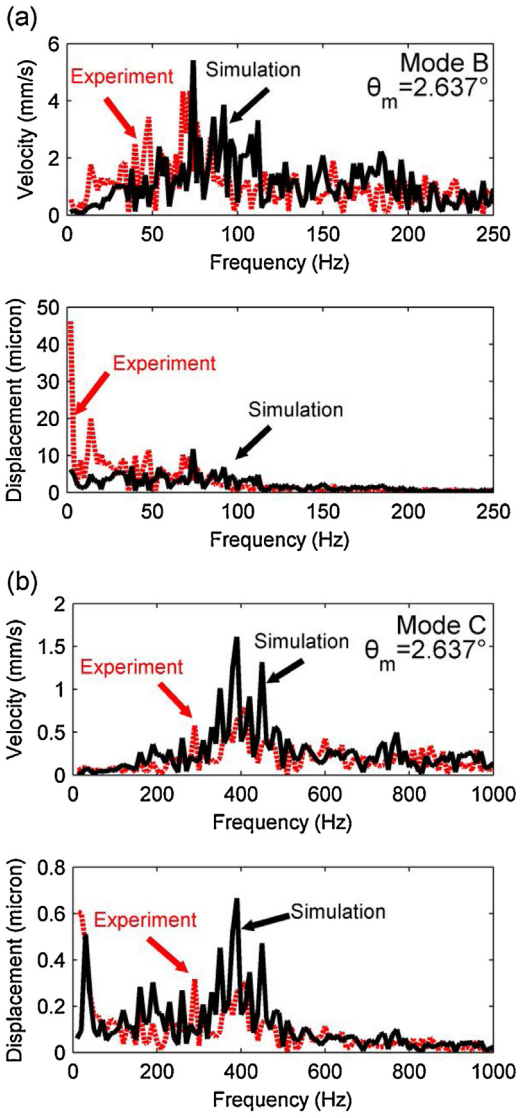

Fig. 9. Frequency spectrum of simulated (black solid line) and experimental (red dash line) velocity and displacement; mode shift angle is 2.635° (a) mode B and (b) mode C. (For interpretation of the references to color in this figure legend, the reader is referred to the web version of this article.)

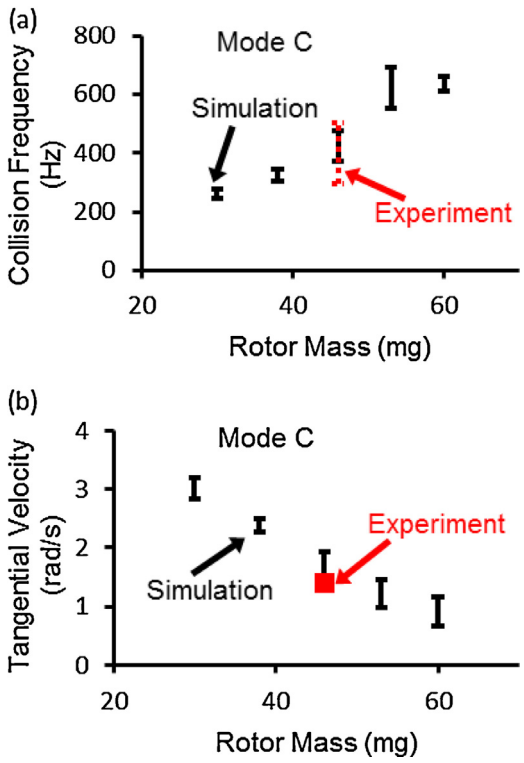

Fig. 10. Mode C (a) collision frequency with different rotor mass and (b) tangential velocity with different rotor mass.

shifting the total angle from 62.135° to 58.135° changes the collision frequency from 101 to 85 Hz, and the rotor tangential velocity from 9.05 to 7.14 rad/s. Similarly, in mode C, shifting the total angle from 62.135° to 58.135° changes the collision frequency from 705 to 314 Hz, and the rotor tangential velocity from 0.75 to 3.03 rad/s.

4. Experimental validation

4.1. Experimental design & setup

An experimental system was used to check the reliability of the simulation for the prototype micro-motor. The magnetoelastic layer was actuated with dual Helmholtz coils that directed an oscillating magnetic field in the same plane as the magnetoelastic layer. The magnetoelastic layer was magnetically biased using small permanent magnets oriented in the same direction as the oscillating field. Vertical motions of multiple points on the unloaded stator are measured by a Laser Doppler Vibrometer (LDV, Polytec OFV 303 sensor head and a Polytec OFV 3001 S vibrometer controller) to check the accuracy of the stator FEM model. The amplitude of the magnetic field generated by the coils at the position of the motor is measured by a gaussmeter (F.W. Bell model 5170) as 8 Oe, typically. A microscope with a high-speed camera (Photron FASTCAM MC2.1 & LEICA 104459290.5x) was used to track rotation of the rotor. The resolution of the camera, when used in conjunction with a microscope, was approximately 2 μm. The frame rate of the camera was as high as 10,000 frames per second.

4.2. Experimental results

4.2.1. Velocity and displacement

Results from experimental measurement of vertical rotor velocity are shown in Fig. 8 for modes B and C, respectively. The displacement of the rotor is calculated by integrating the velocity over time (shown in Fig. 8). As for simulations, an FFT is applied to the experimental measurements. The peak frequency in the resulting FFT spectrum is considered the representative collision frequency for the data set. The amplitude at the peak frequency is also a point of comparison between the simulated and measured results. Tangential velocities are measured by the high-speed camera at frame rates of 5000 fps (mode B) and 10,000 fps (mode C).

4.2.2. Tuning of parametric model

As shown in Table 2, the output of the model is relatively insensitive to shifts in many of the available tuning parameters – coefficient of friction, coefficient of restitution, and squeeze film damping coefficient. However, one tuning parameter that does have significant influence on the model output is the mode shift angle. For mode B, in steady state the frequency of the vertical motion is always around 80 Hz regardless of the mode shift angle. Meanwhile, for mode C, the frequency decreases while the shift angle increases. Considering that the measured collision frequency for mode C is around 400 Hz, tuning the mode shift angle to a value between −2.5° and −3° results in a good match between simulated

Table 3
Simulation and experiment comparison.

Rotor behavior	Simulated	Experiment
Mode B collision frequency	88.8 ± 7.13 Hz	76 ± 20 Hz
Mode B collision amplitude	4.08 ± 1.17 mm/s	3.94 ± 0.57 mm/s
Mode B tangential velocity	8.16 ± 0.80 rad/s	~1 rad/s
Mode C collision frequency	422 ± 51.8 Hz	400 ± 104 Hz
Mode C collision amplitude	1.48 ± 0.26 mm/s	0.88 ± 0.28 mm/s
Mode C tangential velocity	1.72 ± 0.22 rad/s	~1.4 rad/s

and experimentally measured collision frequencies. Therefore, in the following comparison, the mode shift angle in the simulation is set to −2.635°, which makes the sum of the tooth position angle and mode shift angle 30°. The collision frequency and frequency spectrum of vertical motion is well predicted for both mode B and mode C, as shown in Table 3 and Fig. 9. The averages and standard deviations of the presented data are based on the sampling of five simulated and three experimental data sets. The average simulated vertical rotor velocities of both mode B and mode C are larger than average of the experimental results, although standard deviations do significantly overlap. These small differences may be caused by not including in the model all sources of friction on the rotor (e.g., friction between the hub and the rotor).

Meanwhile, the tangential velocities of modes B and C are not equally well predicted. For mode C, the predicted tangential velocity is slightly smaller than the measurement. This is within expected errors due to the sensitivity of simulated results to the exact mode shape and mode shift angle. However, tangential velocity for mode B is substantially over-estimated. This is believed to be due to the stator motion of mode B (about 20 μm amplitude) being much larger than the motion of the mode C (about 1.8 μm amplitude), which leads to non-ideal effects such as rotor wobbling and tilting. Rotor wobble, tilt, and hub collisions are effects not included in the dynamic model; the presence of these effects in the experimental measurements, much more prominently for mode B, are believed to be the primary cause of the discrepancies between the experiment and simulations.

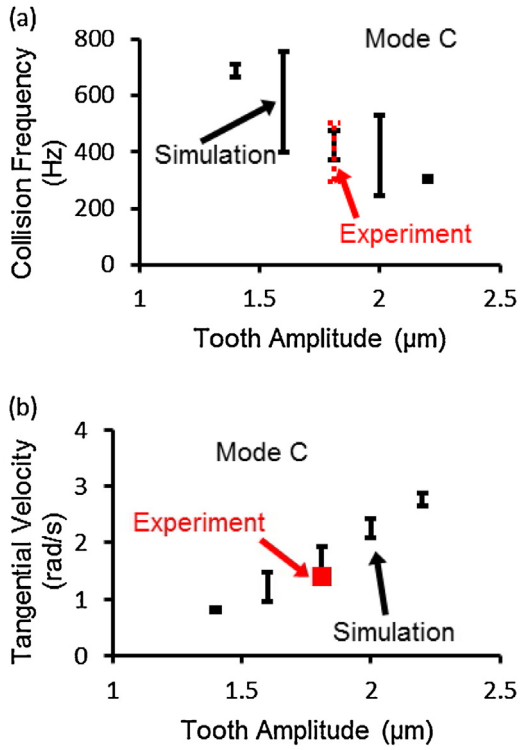

Fig. 11. Mode C (a) collision frequency under different tooth amplitude: simulation (black solid line) and experiment (red dash line) and (b) tangential velocity under different tooth amplitude: simulation (black solid line) and experiment (red dot). (For interpretation of the references to color in this figure legend, the reader is referred to the web version of this article.)

4.3. Sensitivity to payload and stator amplitude

Using the parametric modal model, it is possible to predict the collision frequency and tangential velocity of the rotor under varying actuation conditions including a different payload (rotor mass) and different driving magnetic field strength (tooth amplitude) for the two actuation frequencies. By using the parameters defined in last section, collision frequencies and tangential velocities are simulated, as shown in Figs. 10 and 11, with different rotor masses and tooth amplitudes.

For mode C (Figs. 10 and 11), the collision frequency has a roughly linear relationship with rotor mass and tooth amplitude; the collision frequency increases with increasing rotor mass and decreases with increasing tooth amplitude. The tangential velocity also has a linear relationship with rotor mass and tooth amplitude, and the relationships are the inverse of those for collision frequency. The experimental results fit the simulation within the range of error, indicating that the parametric modal model can be a useful tool for predictive design.

5. Conclusion

This paper develops a dynamic model for a chip-scale magnetoelastic rotary motor actuated by generating a standing wave in a magnetoelastic stator, with momentum transferred to a continuously revolving rotor through collisions with a finite number of stator-located teeth. The stator is treated as a distributed second order linear system excited by a magnetoelastic field, and the response of individual vibrational modes are tracked and summated to determine the total movement of the stator in response to a driving magnetic field and to collisions with the rotor. The dynamic model demonstrated in this paper can qualitatively predict most features of the motor behavior observed in experiments. By tuning a small number of parameters, the model can also achieve a very good quantitative fit to experimentally observed tangential and vertical motion of the rotor under certain actuating conditions.

The dynamic model has substantial benefits for magnetoelastic rotary motor design in allowing the effects of various parameters to be quantified. The stator mass and the tooth height will affect the collision frequency most, while the tangential velocity is affected primarily by the stator mass and mildly by coefficient of friction. The stator thickness, coefficient of restitution and squeeze film damping coefficient are less important for the rotor dynamics.

However, the model still lacks some phenomena that influence motor behavior. For example, for mode B in the prototype system, the simulated and experimental results for tangential velocity do not match well, highlighting one limitation of the model: first, larger stator and rotor motion may lead to unbalanced rotor movement and hub collisions, which are not included in the model. In addition, certain model parameters are difficult to predict before building a motor, especially friction between teeth and the rotor or the hub and the rotor. Future modeling work may include tracking each of four teeth separately (and the necessary asymmetrical mode shapes). This modification could allow the model to include the tilting of the rotor, which may capture small but important aspects of the dynamic motor behavior. Modeling of the contact between the rotor and hub in the current motor design may be more complex; improving the motor design to mitigate this contact – either through a longer hub or by constraining the vertical rotor motion – may be a more practical approach.

Acknowledgements

The authors thank Prof. Karl Grosh for providing access to a Laser Vibrometer used in testing. This work is supported by DARPA MTO, contract W31P4Q-12-1-0002 (PASCAL Program).

References

[1] J. Tang, S.R. Green, Y.B. Gianchandani, Miniature wireless magnetoelastic resonant motor with frequency selectable bidirectional rotation, J. Microelectromech. Syst. 22 (2013) 730–738.
[2] L.-S. Fan, Y.-C. Tai, R.S. Muller, IC-processed electrostatic micromotors, Sens. Actuators 20 (1989) 41–47.
[3] K. Uchino, Piezoelectric ultrasonic motors: overview, Smart Mater. Struct. 7 (1998) 273.
[4] R. Moroney, R. White, R. Howe, Ultrasonic micromotors: physics and applications, in: Micro Electro Mechanical Systems 1990. Proceedings, An Investigation of Micro Structures, Sensors, Actuators, Machines and Robots IEEE, IEEE1990, 1990, pp. 182–187.
[5] M.L. Chan, B. Yoxall, H. Park, Z. Kang, I. Izyumin, J. Chou, et al., Design and characterization of MEMS micromotor supported on low friction liquid bearing, Sens. Actuators A: Phys. 177 (2012) 1–9.
[6] T. Wang, C. Lancée, R. Beurskens, J. Meijer, B. Knapen, A.F. van der Steen, et al., Development of a high-speed synchronous micro motor and its application in intravascular imaging, Sens. Actuators A: Phys. 218 (2014) 60–68.
[7] T. Hosobata, A. Yamamoto, T. Higuchi, An electrostatic induction motor utilizing electrical resonance for torque enhancement, Sens. Actuators A: Phys. 173 (2012) 180–189.
[8] X. Lu, J. Hu, L. Yang, C. Zhao, A novel dual stator-ring rotary ultrasonic motor, Sens. Actuators A: Phys. 189 (2013) 504–511.
[9] N. Yazdi, F. Ayazi, K. Najafi, Micromachined inertial sensors, Proc. IEEE 86 (1998) 1640–1659.
[10] K. Shcheglov, C. Evans, R. Gutierrez, T.K. Tang, Temperature dependent characteristics of the JPL silicon MEMS gyroscope, in: Aerospace Conference Proceedings, 2000 IEEE, 2000, pp. 403–411.
[11] Y.-C. Tai, L.-S. Fan, R.S. Muller, IC-processed micro-motors: design, technology, and testing, in: Micro Electro Mechanical Systems, 1980. Proceedings, An Investigation of Micro Structures, Sensors, Actuators, Machines and Robots IEEE, IEEE1989, 1989, pp. 1–6.
[12] S.F. Bart, M. Mehregany, L.S. Tavrow, J.H. Lang, S.D. Senturia, Electric micromotor dynamics, IEEE Trans. Electron Devices 39 (1992) 566–575.
[13] A. Endemano, J. Fourniols, H. Camon, A. Marchese, S. Muratet, F. Bony, et al., VHDL–AMS modelling and simulation of a planar electrostatic micromotor, J. Micromech. Microeng. 13 (2003) 580.
[14] I. Dufour, E. Sarraute, A. Abbas, Optimization of the geometry of electrostatic micromotors using only analytical equations, J. Micromech. Microeng. 6 (1996) 108.
[15] J. Maas, P. Ide, N. Frohleke, H. Grotstollen, Simulation model for ultrasonic motors powered by resonant converters, in: Industry Applications Conference, 1995. Thirtieth IAS Annual Meeting, IAS'95, Conference Record of the 1995 IEEE, IEEE1995, 1995, pp. 111–120.
[16] N.W. Hagood IV, A.J. McFarland, Modeling of a piezoelectric rotary ultrasonic motor, IEEE Trans. Ultrason. Ferroelectr. Freq. Control 42 (1995) 210–224.
[17] J. Maas, T. Schulte, N. Frohleke, Model-based control for ultrasonic motors, IEEE/ASME Trans. Mechatron. 5 (2000) 165–180.
[18] A. Frangi, A. Corigliano, M. Binci, P. Faure, Finite element modelling of a rotating piezoelectric ultrasonic motor, Ultrasonics 43 (2005) 747–755.
[19] D. Sun, J. Liu, X. Ai, Modeling and performance evaluation of traveling-wave piezoelectric ultrasonic motors with analytical method, Sens. Actuators A: Phys. 100 (2002) 84–93.
[20] W.-M. Zhang, G. Meng, D. Chen, J.-B. Zhou, J.-Y. Chen, Nonlinear dynamics of a rub-impact micro-rotor system with scale-dependent friction model, J. Sound Vib. 309 (2008) 756–777.
[21] G. Meng, W.-M. Zhang, H. Huang, H.-G. Li, D. Chen, Micro-rotor dynamics for micro-electro-mechanical systems (MEMS), Chaos Solitons Fractals 40 (2009) 538–562.
[22] A. Iino, K. Suzuki, M. Kasuga, M. Suzuki, T. Yamanaka, Development of a self-oscillating ultrasonic micro-motor and its application to a watch, Ultrasonics 38 (2000) 54–59.
[23] ASM Handbook, ASM International, 1989.
[24] I. Metglas, Magnetic Alloy 2826MB (nickel-based) Technical Bulletin.
[25] C.C. Lee, C.Y. Wang, G. Matijasevic, Au–In bonding below the eutectic temperature, IEEE Trans. Compon. Hybrids Manuf. Technol. 16 (1993) 311–316.
[26] W.W. So, C.C. Lee, Fluxless process of fabricating In–Au joints on copper substrates, IEEE Trans. Compon. Packag. Technol. 23 (2000) 377–382.
[27] K. Takahata, Y.B. Gianchandani, Batch mode micro-electro-discharge machining, J. Microelectromech. Syst. 11 (2002) 102–110.
[28] J. Benatar, A. Flatau, FEM implementation of a magnetostrictive transducer, in: Smart Structures and Materials, International Society for Optics and Photonics, 2005, pp. 482–493.
[29] S.F. Foerster, M.Y. Louge, H. Chang, K. Allia, Measurements of the collision properties of small spheres, Phys. Fluids (1994-present) 6 (1994) 1108–1115.
[30] W.-M. Zhang, G. Meng, Numerical simulation of sliding wear between the rotor bushing and ground plane in micromotors, Sens. Actuators A: Phys. 126 (2006) 15–24.
[31] M. Behzad, M. Alvandi, D. Mba, J. Jamali, A finite element-based algorithm for rubbing induced vibration prediction in rotors, J. Sound Vib. 332 (2013) 5523–5542.
[32] S. Demiri, Geometric Effects on the Wear of Microfabricated Silicon Journal Bearings, 2010.
[33] A.P. Lee, A.P. Pisano, Repetitive impact testing of micromechanical structures, Sens. Actuators A: Phys. 39 (1993) 73–82.
[34] B. Bhushan, Nanotribology and nanomechanics of MEMS devices, in: Micro Electro Mechanical Systems, 1996. MEMS'96, Proceedings' An Investigation of Micro Structures, Sensors, Actuators, Machines and Systems' IEEE, The Ninth Annual International Workshop on, IEEE1996, 1996, pp. 91–98.
[35] B. Bhushan, X. Li, Micromechanical and tribological characterization of doped single-crystal silicon and polysilicon films for microelectromechanical systems, J. Mater. Res. 12 (1997) 54–63.
[36] M. Bao, H. Yang, Squeeze film air damping in MEMS, Sens. Actuators A: Phys. 136 (2007) 3–27.
[37] W. Griffin, H.H. Richardson, S. Yamanami, A study of fluid squeeze-film damping, J. Basic Eng. 88 (1966) 451.
[38] M.Y. Okiishi, B. Munson, D. Young, Fundamentals of Fluid Mechanics, John Wiley & Sons, Inc., 2006.

Biographies

Jinhong Qu received a B.S. (2011) in engineering physics from the University of Michigan, Ann Arbor, a B.S. (2011) in mechanical engineering from Shanghai Jiao Tong University, Shanghai, China, and a M.S. (2012) in mechanical engineering from the University of Michigan, Ann Arbor. He is currently a doctoral student at the University of Michigan. His research interests include the design, sensing, and control of MEMS devices.

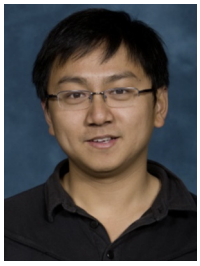

Jun Tang received the B.S. degree in electronic science and technology from Huazhong University of Science and Technology, Wuhan, China, in 2007 and the M.S. degree in microelectronics and solid-state electronics from Shanghai Jiao Tong University, Shanghai, China, in 2010. He received the Ph.D. degree in the Department of Mechanical Engineering from University of Michigan, Ann Arbor, MI, USA, with a focus on microelectromechanical systems. His Ph.D research interests include wireless magnetoelastic sensors and actuators. He is currently a MEMS designer at Freescale Semiconductor Inc., Tempe, Arizona.

Yogesh B. Gianchandani is a Professor at the University of Michigan, Ann Arbor, with a primary appointment in the Electrical Engineering and Computer Science Department and a courtesy appointment in the Mechanical Engineering Department. He also serves as the Director for the Center for Wireless Integrated MicroSensing and Systems ($WIMS_2$).
Dr. Gianchandani's research interests include all aspects of design, fabrication, and packaging of micromachined sensors and actuators (http://www.eecs.umich.edu/~yogesh/). He has published over 300 papers in journals and conferences, and has over 40 US patents issued or pending. He was a Chief Co-Editor of *Comprehensive Microsystems: Fundamentals, Technology, and Applications*, published in 2008. Dr. Gianchandani has served on the editorial boards and program committees of a number of conferences and journals. From 2007 to 2009 he also served at the National Science Foundation, as the program director for Micro and Nano Systems within the Electrical, Communication, and Cyber Systems Division (ECCS). Dr. Gianchandani is a Fellow of IEEE. Dr. Gianchandani is a Fellow of IEEE.

Kenn R. Oldham is an Associate Professor of Mechanical Engineering at the University of Michigan. Prof. Oldham received the Ph.D. in Mechanical Engineering from the University of California at Berkeley in 2006 and the B.S. in Mechanical Engineering from Carnegie Mellon University in 2000. He joined the University of Michigan in 2007 following a post-doctoral fellowship at the Army Research Laboratory. Prof. Oldham and his research group study the intersection of control systems and micro-scale sensing and actuation, with interests in design for controllability, optimal and robust control, and novel sensor and actuator design. Applications of this research include terrestrial micro-robotics, endoscopic microscopy, and inertial and physiological sensing.

Scott R. Green received a B.S. in mechanical engineering from Rose-Hulman Institute of Technology in 2003, and an M.S. (2008) and Ph.D (2009) in mechanical engineering from the University of Michigan, Ann Arbor, with a focus in Microsystems. He worked as a senior design engineer at Stryker Corporation in the Instruments division from 2003-2005 developing minimally invasive surgical devices for vertebroplasty and discectomy procedures. He currently is an Assistant Research Scientist at the University of Michigan, Ann Arbor. Research interests include wireless magnetoelastic sensors and actuators, miniature implantable medical systems, and miniature and microfabricated high-vacuum sputter ion pumps.